Aliovalent doping strategies for enhancing ionic conductivity in Li_3OCl solid electrolytes: a first-principles assessment

Alexander G. Squires, Jacob M. Dean, and Benjamin J. Morgan*

Department of Chemistry, University of Bath, Claverton Down BA2 7AY, United Kingdom and
The Faraday Institution, Quad One, Harwell Science and Innovation Campus, Didcot OX11 0RA, United Kingdom

(Dated: August 12, 2021)

Aliovalent doping of solid electrolytes with the intention of increase the concentration of charge-carrying mobile defects is a common strategy for enhancing their ionic conductivities. For the antiperovskite lithium-ion solid electrolyte Li_3OCl, both supervalent (donor) and subvalent (acceptor) doping schemes have previously been proposed. The effectiveness of these doping schemes depends on two conditions: first, that aliovalent doping promotes the formation of mobile lithium vacancies or interstitials rather than competing immobile defects; and second, that any increase in lithium defect concentration gives a corresponding increase in ionic conductivity. To evaluate the effectiveness of aliovalent doping in Li_3OCl, we have performed a hybrid density-functional theory study of the defect chemistry of Li_3OCl and the response to supervalent and subvalent doping. In nominally stoichiometric Li_3OCl the dominant native defects are predicted to be V_{Li}, O_{Cl}, and V_{Cl}. Supervalent doping increases V_{Li} and O_{Cl} concentrations, with the preferentially-formed defect species dependent on synthesis conditions. Subvalent doping increases the concentration of V_{Cl} more than the concentration of Li_i under all accessible synthesis conditions. While supervalent doping is predicted to be effective at increasing ionic conductivity, particularly under Li-poor synthesis conditions, subvalent doping is predicted to decrease room-temperature ionic conductivities at low-to-moderate doping levels. This effect is due to a reduction in the number of lithium vacancies formed during synthesis, and increased $\left[V'_{Li} + Li_i^\bullet\right]$ Frenkel-pair recombination upon cooling to room temperature. The strongly asymmetric doping response of Li_3OCl with respect to supervalent versus subvalent doping is explained as a consequence of the low $[V_{Li} + V_{Cl}]$ Schottky pair formation energy, suggesting analogous behaviour should be expected in other Schottky-disordered solid electrolytes.

I. INTRODUCTION

All-solid-state lithium-ion batteries that use ion-conducting ceramics as electrolytes have the potential to replace commercial lithium-ion cells that use liquid electrolytes, offering improved energy densities and reliability [1, 2]. A practical solid electrolyte should have a high ionic conductivity to allow fast charge and discharge rates and high power output. To achieve this goal, considerable research effort has been directed towards both the discovery of new materials with intrinsically high ionic mobilities [3–6] and to deriving general principles that can explain how chemical or structural variations within solid electrolytes modulate lithium transport [7–10].

For solid electrolytes in which ionic transport is effected by the diffusion of mobile point defects, one strategy for increasing the ionic conductivity is to increase the concentrations of the charge-carrying defect species through aliovalent doping [11–13], i.e., introducing dopant atoms with a formal valence that differs from that of the atoms being replaced. This difference in effective atomic charge causes a shift in the defect-formation equilibria for all charged native defects, which results in an increase, or decrease, in the concentrations of any charge-carrying vacancies or interstitials.

The effectiveness of aliovalent doping to enhance ionic

conductivity through increasing the concentrations of charge-carrying mobile defects depends on two conditions. First, aliovalent doping should preferentially increase the concentrations of charge-carrying mobile defects ahead of competing immobile defects. For lithium-ion solid electrolytes, doping should preferentially increase the concentration of either lithium vacancies or lithium interstitials. Second, any increase in the concentration of charge-carrying defects should produce a corresponding increase in ionic conductivity. This may not be the case if the ionic conductivity has some dependence on defects other than those being targeted through doping. In solid electrolytes that contain more than one charge-carrying defect species, increasing the concentration of the minority defect species may have little practical effect on the overall ionic conductivity. Alternatively, where there are strong interactions between dopant atoms and oppositely charged mobile defect species, these mobile defects may be kinetically trapped, resulting in a net decrease in ionic conductivity [14, 15]. These potential complications mean that aliovalent doping of solid electrolytes is not guaranteed to produce a significant increase in ionic conductivity, and predicting the effectiveness of a specific aliovalent doping strategy requires characterising the response to doping of all relevant defects in the system of interest.

When considering the response of specific solid electrolytes to aliovalent doping, it is often simply assumed that the introduction of aliovalent dopants is principally charge-compensated by the formation of oppositely

charged *mobile* defect species [11, 14–20]; i.e., in lithium-ion solid electrolytes, supervalent (donor) doping will principally increase the concentration of lithium vacancies and subvalent (acceptor) doping will principally increase the concentration of lithium interstitials. In practice, however, aliovalent doping may instead cause the preferential formation of immobile defects within the host-framework substructure [21], giving much smaller changes in concentrations of the targeted mobile defect species than otherwise would be expected. To accurately predict how defect populations respond to aliovalent doping it is therefore necessary to go beyond simple "charge-compensation" defect schemes, and instead consider a more complete thermodynamic model that accounts for a full range of native defects [21–23].

One lithium-ion solid electrolyte for which a number of aliovalent doping schemes have been proposed is the antiperovskite Li_3OCl [14, 15, 24–26]. Li_3OCl has been widely studied following initial reports of room-temperature ionic conductivities up to $\sim 1 \times 10^{-3}\,\mathrm{S\,cm^{-1}}$[27]. This reported high ionic conductivity is notable because the lithium ions in Li_3OCl are crystallographically ordered; this is in contrast to other high–ionic-conductivity lithium-ion solid electrolytes, such as lithium garnets and lithium thiophosphates, in which lithium is disordered, with this disorder thought to be integral to their fast ion diffusion [8, 28–32].

In Li_3OCl, ionic conductivity is attributed to the diffusion of mobile point defects—specifically lithium vacancies and lithium interstitials [33–36]. Lithium vacancies and interstitials in Li_3OCl are both predicted to be mobile at room temperature, with calculated diffusion barriers of $\sim 0.3\,\mathrm{eV}$ and $\sim 0.15\,\mathrm{eV}$, respectively [33–36]. While these diffusion barriers indicate that lithium interstitials are significantly more mobile than lithium vacancies, calculated defect-pair formation energies give a lower formation energy for $[V_{Li} + V_{Cl}]$ Schottky pairs ($1.0\,\mathrm{eV}$ to $1.6\,\mathrm{eV}$) than for $[V_{Li} + Li_i]$ Frenkel pairs ($1.9\,\mathrm{eV}$ to $2.5\,\mathrm{eV}$) [34, 37, 38], making lithium vacancies the expected dominant charge-carrying defect species in undoped Li_3OCl.

Both supervalent and subvalent doping strategies have been proposed to enhance the ionic conductivity of Li_3OCl [14, 15, 26, 33, 34, 39, 40]. Supervalent doping—e.g., where a cation such as Mg^{2+} or Al^{3+} replaces Li^+—has been proposed as an effective route to increase the concentration of lithium vacancies [15, 26, 33, 34, 39, 40], while subvalent doping—e.g., where an anion such as S^{2-} replaces Cl^-—has been proposed as an effective route to increase the concentration of lithium interstitials [14]; in this case it has been suggested that because of the much higher mobility of interstitials relative to that of the intrinsically dominant lithium vacancies, a relatively small increase in lithium interstitial concentration might produce a disproportionately large increase in ionic conductivity.

Several of the characteristic properties of Li_3OCl—a high degree of crystallographic ordering of mobile ions; low Schottky-pair formation energies, giving much higher concentrations of mobile vacancies than mobile interstitials; and higher mobilities for these interstitials than for corresponding vacancies—are shared by a number of other antiperovskite and structurally-related solid electrolytes [6, 36, 41–44]. Understanding the effectiveness of different aliovalent doping schemes in Li_3OCl is useful, therefore, not only because it may help direct the optimisation of ionic conductivity for this one material, but also because it can provide more general insights into doping responses for this entire class of solid electrolytes.

Here, we describe a hybrid density-functional theory (DFT) study of Li_3OCl that considers all native vacancy, interstitial, and anion antisite defects within a self-consistent thermodynamic model [45, 46], which we have performed in order to characterise the native defect chemistry of Li_3OCl, and to model the effect of supervalent and subvalent doping on native defect concentrations and ionic conductivity.

In undoped, nominally stoichiometric, Li_3OCl we predict that the dominant defect species varies with synthesis conditions; under Li-poor conditions the dominant negative defect species is V'_{Li} and the dominant positive defect species is $V^{\bullet}_{Cl}$; under Li-rich conditions the dominant defect species are O'_{Cl} and $V^{\bullet}_{Cl}$. Under all considered synthesis conditions, we predict lithium vacancies to be present in much greater concentrations than lithium interstitials, in qualitative agreement with previous studies [14, 15, 38, 41, 47, 48], and confirming V_{Li} as the dominant charge carrier in nominally stoichiometric samples.

For doped Li_3OCl, supervalent doping is predicted to increase the concentration of both V_{Li} and O_{Cl}, with the preferentially formed defect depending on synthesis conditions, while subvalent doping is predicted to preferentially increase the concentration of V_{Cl} ahead of Li_i under all considered synthesis conditions.

Supervalent doping is predicted to be effective at increasing the ionic conductivity, particularly under Li-poor synthesis conditions. Subvalent doping at moderate doping levels, however, is predicted to *decrease* the room-temperature ionic conductivity, due to two complementary effects. First, subvalent doping at low-to-moderate dopant concentrations decreases the concentration of lithium vacancies more rapidly than it increases the concentration of lithium interstitials. Second, increasing the number of lithium interstitials formed under synthesis conditions causes increased "quenching" of lithium vacancies when cooling to room temperature through recombination of V_{Li} as $[V_{Li} + Li_i]$ Frenkel pairs. Although sufficiently high levels of subvalent doping are predicted to increase ionic conductivity relative to undoped Li_3OCl, the ionic conductivity thus obtained is significantly lower than predicted for supervalent doping at equivalent dopant concentrations. We therefore do not expect subvalent doping to be a practical doping strategy for increasing the ionic conductivity of Li_3OCl.

Finally, we discuss how the strongly asymmetric dop-

ing response of Li_3OCl can be understood as a consequence of the low $[V_{Li} + V_{Cl}]$ Schottky-pair formation energy, and how this implies qualitatively similar doping response behaviours for other Schottky-disordered solid electrolytes, including other antiperovskite and structurally-related materials.

II. METHODS

A. Thermodynamically self-consistent defect calculations

For non-interacting defects, the concentration of defect X in charge state q is given by

$$[X^q] = N_X \, g_{X,q} \, \exp\left(\frac{-\Delta E_f^{X^q}}{kT}\right), \qquad (1)$$

where N_X is the density of sites at which X can form, $g_{X,q}$ is the degeneracy of the defect charge state (e.g. spin degeneracy), k is the Boltzmann constant, T is the temperature, and $\Delta E_f^{X^q}$ is the formation energy of defect X in charge state q [46, 49]. Defect formation energies are calculated as

$$\Delta E_f^{X^q} = E_{tot}^{X^q} - E_{tot}^{bulk} - \sum_i n_i(\mu_i + \Delta\mu_i) \qquad (2)$$
$$+ q(E_F + E_{vbm} + \Delta V_{pot}) + E_{corr}^q,$$

where $E_{tot}^{X^q}$ is the total energy of a supercell containing defect X in charge state q, and E_{tot}^{bulk} is the total energy of the defect free supercell. $\Delta\mu_i$ are chemical potentials of each atomic species i that are added to ($n_i > 0$) or removed from ($n_i < 0$) the supercell to form defect X. μ_i are elemental reference energies, calculated for each element in its standard state. E_F is the Fermi energy, with this term accounting for the energy to add ($q < 0$) or remove ($q > 0$) electrons to or from the supercell. E_{vbm} is the DFT-calculated energy of the valence-band maximum of the host system. ΔV_{pot} is a potential alignment term that accounts for differences in background electrostatic potentials between the host and defective supercells [45]. E_{corr}^q is a correction term accounting for the finite size of the supercell. Image-charge corrections were determined using the method of Lany and Zunger [50] and electrostatic potentials were aligned with respect to average core potentials for sets of atoms far from the defect.

When calculating defect formation energies using eq. (2), the Fermi energy, E_F, is determined self-consistently by solving eqs. (1) and (2) under the constraint of net charge neutrality [46, 49]. The net charge density of a system, ρ, is calculated as a sum over all defect species (X) and their charges (q) plus the charge contributions from free electrons (n_0) and holes (p_0) that are considered to occupy the conduction and valence bands

respectively,

$$\rho = \sum_{X^q} q[X^q] + p_0 - n_0 \qquad (3)$$
$$\equiv 0.$$

Electron and hole populations are determined from the relevant Fermi-Dirac distributions,

$$n_0 = \int_0^\infty \frac{1}{e^{(E-E_F)/kT} + 1} g(E) \, dE, \qquad (4)$$

$$p_0 = \int_0^\infty 1 - \frac{1}{e^{(E-E_F)/kT} + 1} g(E) \, dE, \qquad (5)$$

where $g(E)$ is the bulk density of states [51].

In the absence of significant short-ranged dopant—defect interactions, aliovalent doping can be modelled as a perturbation to the electroneutrality condition (eq. (3)).

$$\rho(E_F, r[M^r]) = \sum_{X^q} q[X^q] + p_0 - n_0 + r[M^r], \qquad (6)$$

where M is an aliovalent dopant with relative charge r and fixed concentration $[M^r]$ [21]. In the dilute limit, this doping response does not depend explicitly on the dopant species and insertion site, but only on the product $r[M^r]$.

B. DFT calculation methodology

To calculate defect formation energies in Li_3OCl, we have performed a series of hybrid-DFT calculations using the plane-wave DFT code VASP [52, 53] using the HSE06 hybrid functional [54]. Hybrid DFT typically gives more accurate descriptions of electronic structure than conventional pure-LDA or GGA functionals [55] while also approximately correcting for the self-interaction error exhibited by local or semi-local functionals; the self-interaction error can lead to unphysical delocalisation of charge for defects in wide-gap oxides giving a qualitatively incorrect description of different defect charge states [21, 56–59]. All calculations used a plane-wave basis cutoff of $520\,eV$ and defect calculations were performed using a $3 \times 3 \times 3$ supercell of the Li_3OCl unit cell. Interactions between core and valence electrons were described using the projector augmented wave method [60] with cores of [H] for Li, [He] for O and [Ne] for Cl. To avoid spurious forces associated with Pulay stress, equilibrium volumes were calculated using a series of constant volume calculations and fitted to the Murnaghan equation of state [61]. Geometry optimisations were deemed converged when all atomic forces were smaller than $1 \times 10^{-3}\,eV/Å$. Supercell calculations used a $2 \times 2 \times 2$ Monkhorst-Pack grid for sampling **k**-space.

Our calculations predict a lattice parameter for Li_3OCl of $3.82\,Å$, which slightly underestimates the experimental value of $3.91\,Å$ [27] but is in good agreement with previous DFT calculations [26]. Our calculated value for

the band gap of Li_3OCl of $6.6\,eV$ compares well to previously calculated values of $6.4\,eV$ [26, 34]; To the best of our knowledge the band gap of Li_3OCl has not yet been measured experimentally.

A dataset containing inputs and outputs for all DFT calculations supporting this study is available under the CC-BY-4.0 license from the University of Bath Research Data Archive [62]. Python codes for calculating defect formation energies and defect concentrations as functions of elemental chemical potentials, and Jupyter notebooks used to generate Figures 1 to 8 are available under the MIT license [63]. Our analysis codes use the scipy [64], numpy [65], pandas [66] matplotlib [67] and py-sc-Fermi [68] Python packages. Chemical potential limits stability analysis used the FORTRAN package CPLAP [69].

III. RESULTS

A. Defining a "synthetically accessible" chemical potential space for Li_3OCl

To calculate defect formation energies, and hence predict defect concentrations, it is necessary to define the accessible ranges of chemical potentials for the elemental species involved in the formation of each defect (cf. eq. (2)). In most defect studies, the relevant region of chemical potential space is constrained by the thermodynamic stability limits of the system under study with respect to competing phases [45]. Li_3OCl, however, is not thermodynamically stable, but is metastable with respect to formation of Li_2O and $LiCl$ [34, 70]. Here, we follow the approach of Emly *et al.* and assume that the degradation of Li_3OCl to form Li_2O is kinetically suppressed, and therefore construct a metastable phase diagram with Li_2O removed as a competing phase [34]. The assumption that Li_3OCl is metastable with respect to decomposition to Li_2O and $LiCl$ is supported by a recent analytical and force-field–based atomistic modelling study that predicts excellent kinetic stability of Li_3OCl with respect to this decomposition pathway [71], although experimental synthesis of phase-pure crystalline Li_3OCl remains extremely challenging [43].

Li_3OCl is typically synthesised at $300\,°C$ to $360\,°C$ and under vacuum [27], therefore, to define a "synthetically accessible" chemical potential range for Li_3OCl we further restrict the region of predicted metastability by considering chemical potentials corresponding to these synthesis conditions [72], via

$$\Delta\mu_O(T, P) = \frac{1}{2}\left\{(T - T_0) - \qquad (7)\right.$$
$$\left. T\left[S_0 + C_p \ln\frac{T}{T_0} + k \ln\frac{P}{P_0}\right]\right\}$$

where T and P are synthesis temperatures and pressures respectively and k is the Boltzmann constant. We use the experimental value for the oxygen standard entropy,
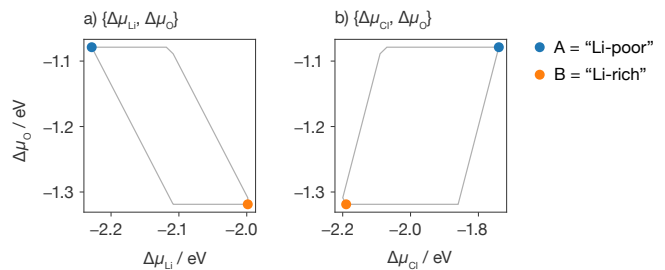
FIG. 1. Two-dimensional projections of the "synthetically accessible" 3D chemical potential space for Li_3OCl. a) $\{\Delta\mu_{Li}, \Delta\mu_O\}$ projection. b) $\{\Delta\mu_{Cl}, \Delta\mu_O\}$ projection. For our defect and doping response calculations we consider the maximally lithium-poor and lithium-rich limits: A $\rightarrow$ $\{\Delta\mu_{Li} = -2.23\,eV, \Delta\mu_{Cl} = -1.75\,eV, \Delta\mu_O = -1.08\,eV\}$, and B $\rightarrow$ $\{\Delta\mu_{Li} = -2.00\,eV, \Delta\mu_{Cl} = -2.19\,eV, \Delta\mu_O = -1.32\,eV\}$, respectively.

$S_0 = 205\,J/mol/K$ [73], and assume that oxygen behaves as an ideal gas and use $C_P = \frac{7}{2}k$ for the constant-pressure specific heat capacity per diatomic molecule [73–75]. The resulting "synthetically accessible" range of elemental chemical potentials defines a three-dimensional region of $\{\mu_O, \mu_{Cl}, \mu_{Li}\}$ chemical-potential space with six vertices (fig. 1). Within these six limiting conditions, we explicitly consider the maximally lithium-rich and lithium-poor conditions, which are labelled A and B, respectively, in fig. 1, corresponding to A $\rightarrow$ $\{\Delta\mu_{Li} = -2.23\,eV, \Delta\mu_{Cl} = -1.75\,eV, \Delta\mu_O = -1.08\,eV\}$, and B $\rightarrow$ $\{\Delta\mu_{Li} = -2.00\,eV, \Delta\mu_{Cl} = -2.19\,eV, \Delta\mu_O = -1.32\,eV\}$. Full details of the calculations used to determine these chemical potential limits are provided in the supporting data set [62].

B. Intrinsic defect chemistry of undoped Li_3OCl

We first consider the formation energies and equilibrium concentrations of native defects in undoped, nominally stoichiometric, Li_3OCl. Figure 2 shows formation energies of native defects in Li_3OCl as a function of Fermi energy, under Li-poor and Li-rich conditions (upper panels), and the corresponding equilibrium defect concentrations (lower panels). Under Li-poor conditions, the dominant defect species are lithium vacancies, V_{Li}, and chlorine vacancies, V_{Cl}, which is qualitatively consistent with previous predictions of Li_3OCl as being predominantly $[V_{Li} + V_{Cl}]$ Schottky-disordered [34, 37, 38]. The dominant $[V_{Li} + V_{Cl}]$ Schottky disorder can also be assigned directly from the defect formation energies plot (fig. 2(a)), which shows the equilibrium Fermi energy is "pinned" by the V'_{Li}–$V^{\bullet}_{Cl}$ defect pair. Under Li-rich conditions, chlorine vacancies, $V^{\bullet}_{Cl}$, are the dominant positively charged defect species. The dominant negatively charged defect, however, is now the oxygen–chlorine antisite, O'_{Cl}. From a charge- and mass-balanced defect
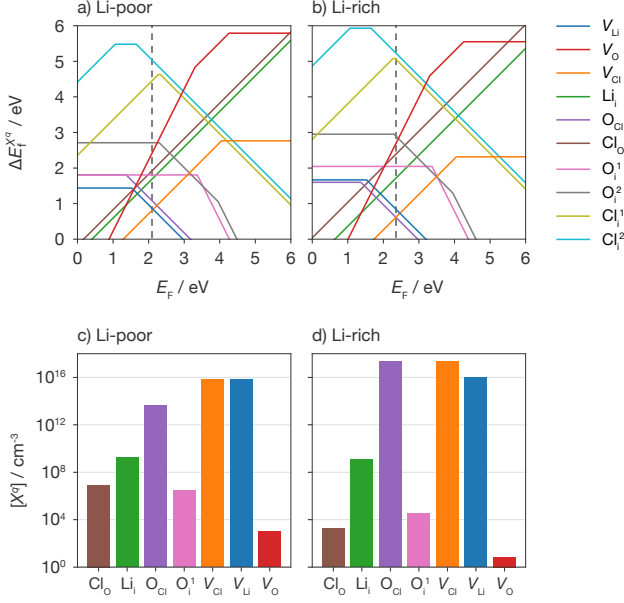
FIG. 2. Defect formation energies (top) and defect concentrations (bottom) for defects in Li_3OCl under Li-poor and Li-rich synthesis conditions (see fig. 1), at 360 °C. The dashed line marked on the transition level diagrams is the position of the self-consistently determined Fermi energy; defect charge states are given by the gradient. For the defect concentration plots we show only those defect species with concentrations $[X] > 1 \times 10^2 \, \mathrm{cm^{-3}}$ under Li-rich or Li-poor conditions. Defect species with concentrations $[X] < 1 \times 10^2 \, \mathrm{cm^{-3}}$ under all conditions are not shown in the bottom plots.

FIG. 3. Defect formation energies (top) and defect concentrations (bottom) for defects in undoped and supervalent doped Li_3OCl under lithium poor (left) and lithium rich (right) conditions (see fig. 1), at 360 °C. In the upper panels, the vertical dashed line shows the equilibrium Fermi energy in the undoped system, and the vertical solid line shows the equilibrium Fermi energy when doping at an effective dopant concentration of $r[M^r] = 10^{18} \, \mathrm{cm^{-3}}$ (see eq. (6)) [80]. Defect species with concentrations $[X] < 1 \times 10^2 \, \mathrm{cm^{-3}}$ under all conditions are not shown in the bottom plots.

reaction perspective the system is no longer best characterised by $[V_{Li} + V_{Cl}]$ Schottky disorder, and the lowest energy defect-formation reaction is

$$Li_2O + 2Cl_{Cl}^\times \rightarrow O_{Cl}' + V_{Cl}^\bullet + 2LiCl. \quad (8)$$
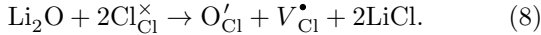
This different classification can again be assigned from the plot of Fermi-energy dependent defect formation energies, where the Fermi energy is now pinned by the O_{Cl}'–$V_{Cl}^\bullet$ defect pair (fig. 2(b)).

The presence of anion disorder in Li_3OCl in the form of O_{Cl} antisites, particularly under Li-rich conditions, has potential implications for lithium transport. $[O_{Cl}' + Cl_O^\bullet]$ antisite pairs have been predicted via *ab initio* molecular dynamics to enhance lithium diffusion relative to a perfectly anion-ordered reference system [33]. Anion framework disorder has also been associated with increased ionic conductivity in other antiperovskites [76, 77] and in other lithium-ion solid electrolytes [8, 78, 79]. Synthesis protocols that increase the degree of host-framework–disorder in Li_3OCl, or in other antiperovskites, may therefore provide alternative routes to improving the ionic conductivities of these materials beyond purely modifying lithium stoichiometry.

Although symmetric O/Cl disorder has been predicted to give increased lithium transport [33], our calculations predict that O–Cl antisites in Li_3OCl do not form in stoichiometry-preserving $[Cl_O^\bullet + O_{Cl}']$ pairs, but instead there is a large excess of O_{Cl}' antisites. Previous *ab initio* molecular dynamics simulations have predicted that isolated O_{Cl}' defects electrostatically trap lithium interstitials, thereby suppressing lithium diffusion [14, 38]. In undoped Li_3OCl, however, lithium vacancies are the dominant charge-carrying lithium defect species under all conditions, with lithium interstitial concentrations several orders of magnitude lower. Any trapping of lithium interstitials by O_{Cl}' is therefore expected to have a negligible effect on the net ionic conductivity of undoped Li_3OCl.

C. Supervalent and subvalent doping response in Li_3OCl

We now consider how the intrinsic native defect concentrations in Li_3OCl respond to aliovalent doping. Figure 3 shows, again, the Fermi-energy dependent defect formation energies and equilibrium defect concentrations in as-synthesised Li_3OCl, but now compares these "stoichiometric" defect concentrations with those predicted for an effective supervalent dopant concentration of $r[M^r] = 10^{18} \, \mathrm{cm^{-3}}$ (see eq. (6)) [80]. Supervalent doping under Li-poor conditions principally increases the
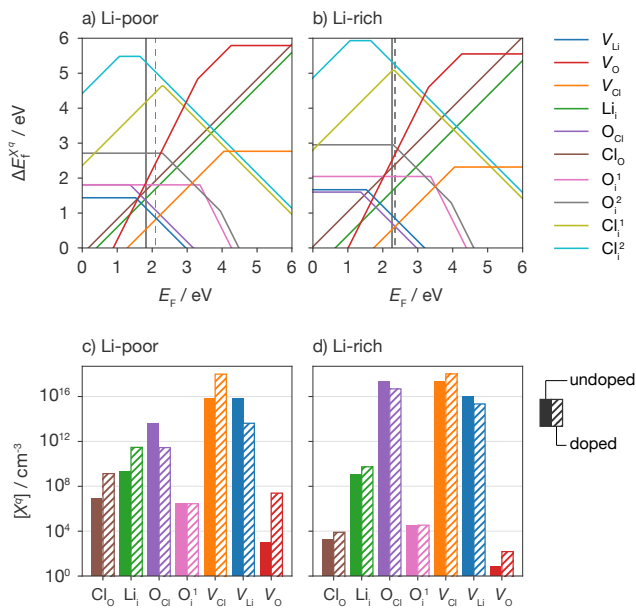
FIG. 4. Defect formation energies (top) and defect concentrations (bottom) for defects in undoped and subvalent doped Li$_3$OCl under lithium poor (left) and lithium rich (right) conditions (see fig. 1), at 360 °C. In the upper panels, the vertical dashed line shows the equilibrium Fermi energy in the undoped system, and the vertical solid line shows the equilibrium Fermi energy when doping at an effective dopant concentration of $r[M^r] = -10^{18}\,\mathrm{cm}^{-3}$. Defect species with concentrations $[X] < 1 \times 10^2\,\mathrm{cm}^{-3}$ under all conditions are not shown in the bottom plots.

concentration of lithium vacancies, which are the lowest formation energy negatively-charged defect species in the parent undoped material—the system therefore behaves qualitatively as predicted by simple lithium-defect charge-compensation models. Supervalent doping under Li-rich conditions principally increases the concentration of the O$'_{\mathrm{Cl}}$ antisite, which is now the lowest formation energy negatively-charged defect species. Under Li-rich conditions, therefore, supervalent doping produces a smaller increase in lithium vacancy concentration than predicted by simple models that assume direct charge-compensation by lithium defects.

The equivalent analysis for the case of subvalent doping is shown in fig. 4. Under both Li-rich and Li-poor synthesis conditions, subvalent doping gives only a modest increase in the concentration of lithium interstitials, and the principal effect is instead to increase the concentration of $V^{\bullet}_{\mathrm{Cl}}$ lithium vacancies. We also observe a significant decrease in the lithium vacancy concentration. Although lithium interstitials are expected to be more mobile than lithium vacancies, this analysis suggests the potential for a regime where subvalent doping causes a net *decrease* in ionic conductivity due to the decrease in the dominant charge-carrying lithium-defect species, i.e., lithium vacancies. We return to this point in more detail in section III D where we quantify how ionic conductivi-

ties are predicted to vary as a function of supervalent or subvalent dopant concentrations.

The results above highlight how aliovalent doping of solid electrolytes can produce qualitatively different responses, depending on the relative concentrations of competing native defects in the parent undoped system. Aliovalent doping introduces excess charge that causes a shift in the Fermi energy of the system and a corresponding shift in the defect equilibria for all charged defect species. The qualitatively different doping responses under different synthesis conditions can be understood by considering how the concentrations of the native defect species respond to a given shift in the Fermi energy, $\Delta E_{\mathrm{F}} = E_{\mathrm{F}}^{\mathrm{doped}} - E_{\mathrm{F}}^{\mathrm{undoped}}$. Assuming that defects do not change charge-state in the range ΔE_{F}, the change in concentration of each defect species, $\Delta[X^q]$, is given by (from Eqns 1 and 2)

$$\Delta[X^q] = [X^q]^{\mathrm{doped}} - [X^q]^{\mathrm{undoped}}$$
$$= [X^q]^{\mathrm{undoped}} \left(\exp\left(\frac{-q\Delta E_{\mathrm{F}}}{kT} \right) - 1 \right). \quad (9)$$

Aliovalent doping therefore produces a change in defect concentration that is proportional to the concentration of that defect species in the undoped material. Simple defect reaction schemes that assume that aliovalent doping is principally charge-compensated by forming additional charge-carrying mobile defects will therefore overestimate the effect of doping at some fixed concentration, unless the mobile defect species being targeted for enhancement is the dominant positively, or negatively, charged native defect species in the corresponding undoped system.

To illustrate this difference in predicted behaviour between a simple charge-compensation model and our full self-consistent model, we consider the doping response of Li$_3$OCl as a function of effective dopant concentration, $r[M^r]$, for both a simple "lithium-only" charge compensation model, where only charge-carrying lithium defects change concentration in response to doping, and for our full model, where all defects re-equilibrate. Figure 5 shows the predicted doping response for these two models, for supervalent doping and subvalent doping at a range of dopant concentrations, under Li-rich and Li-poor synthesis conditions. Here, we have considered a maximum dopant concentration equivalent to $\sim 4\%$ of lithium sites, which is a similar dopant/defect concentration to that used in previous *ab initio* molecular dynamics studies of doping in Li$_3$OCl [14, 33]. Because our model assumes that defects behave ideally (via our use of eq. (1)) our results are expected to be quantitatively accurate only at low dopant and defect concentrations. At high dopant or high defect concentrations, non-ideal defect–defect interactions may make a significant contribution to defect chemical potentials, causing defect concentrations to deviate from the dilute-limit behaviour modelled here [81, 82]. We expect, however, that general trends regarding the relative response of different defects
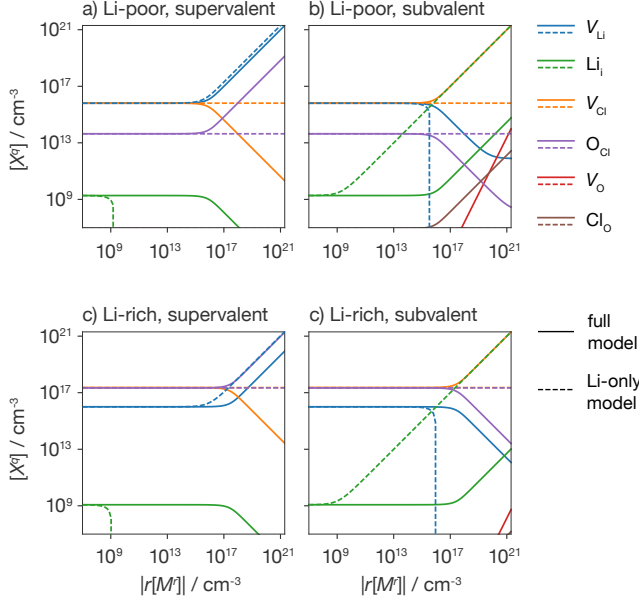
FIG. 5. Defect concentrations as a function of effective dopant concentration $(r[M^r])$ shown for both supervalent dopants (left column), and subvalent dopant (right column), for Li-poor (top row) and Li-rich (bottom row) synthesis conditions, at 360 °C. The solid lines show defect concentrations when all defect concentrations are allowed to vary as the dopant concentration is increased, the dotted lines show the case when only the concentration of lithium defects are allowed to change.

to doping will be qualitatively correct even at these high dopant concentrations.

The only case where the simple "lithium-only" defect model gives approximate quantitative agreement with the full model, with respect to the change in concentrations of charge-carrying lithium defect species, is for supervalent doping under Li-poor synthesis conditions (fig. 5). In this case, the lowest formation energy negatively-charged defect species in the undoped system is the lithium vacancy, which therefore shows the strongest enhancement in concentration under supervalent doping. Under Li-poor conditions, the dominant negatively-charged defect species in the undoped system is the oxygen–chlorine O'_{Cl} antisite, which is now preferentially enhanced by supervalent doping. This suppresses the increase in lithium vacancy concentration relative to that predicted by the simple "lithium-only" model.

Under subvalent doping, the two models give even more strongly divergent predictions; the lithium-only defect model underestimates the doping threshold at which a significant increase in concentration of lithium interstitials is observed by several orders of magnitude. This effect can be understood by considering the conventional "Schottky pair" description of defect disorder in Li_3OCl; the dominant positively charged defect species is the chlorine vacancy, $V_{Cl}^{\bullet}$, and subvalent doping therefore prin-

cipally increases the concentration of this non-charge-carrying host-framework defect ahead of the minority $Li_i^{\bullet}$ defects.

D. Defect mediated ionic conductivity in Li_3OCl

We next consider how the variation in native defect concentrations under different synthesis conditions, and the associated varying response to supervalent and subvalent doping, affects the ionic conductivity of doped Li_3OCl. To estimate the effect of supervalent or subvalent doping on ionic conductivity, we use the Nernst–Einstein relation between ionic conductivity, σ, and self-diffusion coefficient D^*:

$$\sigma = \frac{Cq^2}{kT}D^*, \tag{10}$$

where C and q are the concentration and charge of the mobile ions, respectively, k is the Boltzmann constant, and T is the temperature [83]. We assume lithium diffusion is effected by dilute populations of lithium vacancies and lithium interstitials, which allows us to neglect correlation effects in eq. (10), and also allows us to express the total ionic conductivity as a sum over contributions from lithium vacancies and lithium interstitials respectively:

$$\sigma = \frac{[V_{Li}]}{kT}D^*_{V_{Li}} + \frac{[Li_i]}{kT}D^*_{Li_i}. \tag{11}$$

The self-diffusion coefficients for each defect species are estimated from the dilute limit expression for independent defect hopping

$$D^*_X = \frac{1}{6}\nu_0 a^2 \exp\left(\frac{-\Delta E_X}{kT}\right), \tag{12}$$

where ν_0 is the attempt frequency, which we set as a characteristic value of 1×10^{13} Hz for both lithium vacancies and lithium interstitials, and a is the hop distance [84] which we take as nearest-neighbour Li—Li distance of 2.67 Å. ΔE_X is the potential energy barrier for defect species X to hop between adjacent defect sites, for which we use the barrier heights calculated by Emly et $al.$ of $\Delta E_{Li_i} = 0.17$ eV, $\Delta E_{V_{Li}} = 0.34$ eV [34], which gives a ratio $D^*_{Li_i}/D^*_{V_{Li}} \approx 10^3$ at $T = 298$ K.

To calculate the ionic conductivity of Li_3OCl using eq. (11) we require the lithium vacancy and lithium interstitial concentrations under typical operating conditions. Crucially, these defect concentrations can differ from the values predicted under typical synthesis conditions (300 °C to 360 °C under vacuum) that we have presented in sections III B and III C. Both lithium vacancies and lithium interstitials are highly mobile even at room temperature, and some proportion of lithium vacancy–interstitial pairs will recombine as the temperature is decreased. Electron and hole pairs may also recombine upon cooling, although in a wide-gap system
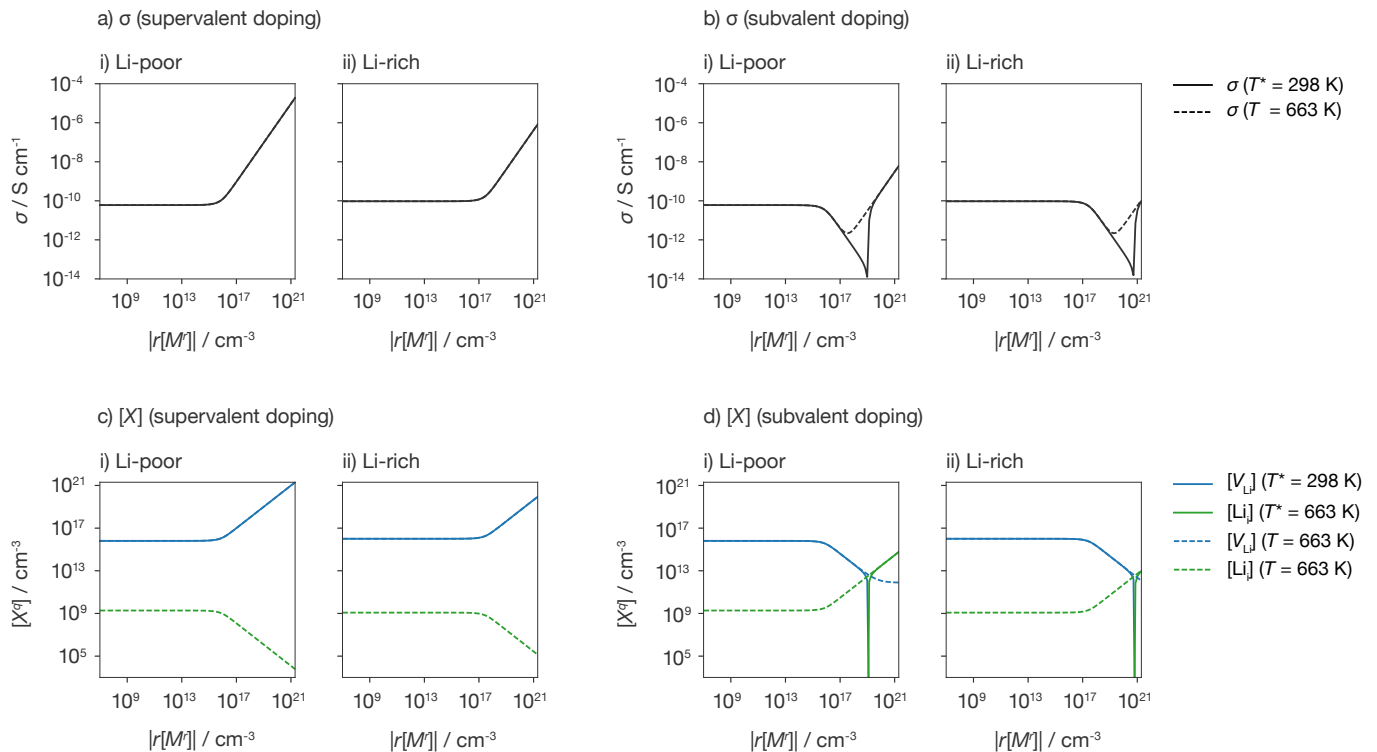
FIG. 6. Ionic conductivities (top panels) and lithium interstitial and lithium vacancy concentrations (bottom panels) as a function of effective doping concentration $r\,[M^r]$ for Li-rich and Li-poor synthesis conditions and for supervalent and subvalent doping. Dashed lines show equilibrium data calculated for synthesis conditions at 663 K. Solid lines show pseudo-equilibrium data calculated at 298 K allowing lithium interstitials and lithium vacancies to re-equilibrate under fixed total lithium content, while other defects are "frozen in" at their synthesis concentrations.

such as Li_3OCl, this is expected to have a negligible effect on the Fermi level position and therefore on defect populations.

To model the change in lithium defect concentration upon cooling from synthesis temperatures to room temperatures, we perform a two-stage calculation. We first calculate equilibrium concentrations for all defect species at a typical synthesis temperature of 360 °C. We then fix the concentrations of all anionic defect species, which are considered to be "frozen in" during cooling [71, 85], and recalculate the lithium vacancy and interstitial concentrations and electron and hole concentrations a pseudo-equilibrium temperature $T^* = 298$ K, under the additional constraint that there is no net lithium exchange with the surroundings [86].

Figure 6 shows calculated lithium vacancy and lithium interstitial concentrations and corresponding ionic conductivities (via eq. (11)) for Li_3OCl synthesised under Li-poor and Li-rich conditions, as a function of supervalent and subvalent effective dopant concentrations. To illustrate the effect of cooling from synthesis conditions to room temperature on lithium defect concentrations and on the ionic conductivity, we show data calculated for full equilibration under synthesis conditions ($T = 663$ K; dashed lines) and for partial re-equilibration at room

temperature ($T^* = 273$ K; solid lines).

For undoped Li_3OCl we predict ionic conductivities of $4.2 \times 10^{-10}\,\mathrm{S\,cm^{-1}}$ under Li-poor synthesis conditions and $6.7 \times 10^{-10}\,\mathrm{S\,cm^{-1}}$ under Li-rich synthesis conditions. In both cases the contribution to the ionic conductivity from lithium interstitials is negligible ($\sim 10^{-14}\,\mathrm{S\,cm^{-1}}$). Our calculated ionic conductivities ($\sim 5 \times 10^{-10}\,\mathrm{S\,cm^{-1}}$) are much lower than those previously reported for experimental samples of nominally stoichiometric Li_3OCl ($10^{-3}\,\mathrm{S\,cm^{-1}}$ to $10^{-6}\,\mathrm{S\,cm^{-1}}$) [27, 87]. One possible reason for this discrepancy is that previous experimental data might not have been obtained for phase-pure "stoichiometric" Li_3OCl. Li_3OCl is extremely challenging to synthesise, as indicated by the small calculated region of metastability under typical synthesis conditions (fig. 1), and it has been suggested that samples reported in the literature as Li_3OCl may in fact be competing hydrated phases, such as Li_2OHCl [43, 88], which are predicted to have higher total conductivities than pristine Li_3OCl [89].

Considering the effect of aliovalent doping on ionic conductivity, supervalent doping produces a monotonic increase in the concentration of lithium vacancies, and therefore also produces a monotonic increase in ionic conductivity. The quantitative effect of supervalent doping

on ionic conductivity depends on synthesis conditions. Under Li-poor conditions, where lithium vacancies are the highest concentration native defect species, the ionic conductivity behaves almost entirely as predicted by assuming direct charge-compensating formation of lithium vacancies. Under Li-rich conditions, however, where the dominant negatively charged native defect species is the oxygen–chlorine antisite O'_{Cl}, this non–charge-carrying defect species is preferentially formed. The positive effect of supervalent doping on ionic conductivity is therefore suppressed, and higher effective dopant concentrations are needed for a given increase in ionic conductivity than predicted by a simple lithium-defect charge-compensation model.

In contrast to the monotonic increase in ionic conductivity produced by supervalent doping, subvalent doping causes the ionic conductivity to *decrease* at moderate effective dopant concentrations under all synthesis conditions. High dopant concentrations are needed to achieve a net increase in ionic conductivity relative to undoped Li_3OCl through subvalent doping. This behaviour is a consequence of two factors. First, although subvalent doping increases the concentrations of all positively-charged defect species, it also decreases the concentrations of all negatively-charged defect species, including lithium vacancies. Because, in the undoped systems, the concentration of lithium vacancies is significantly higher than that of lithium interstitials, low-to-moderate levels of subvalent doping decrease the concentration of lithium vacancies by a much greater extent than they increase the concentration of lithium interstitials (cf. eq. 9). In as-synthesised Li_3OCl, this effect gives a minimum in ionic conductivity when $[V_{Li}] D^*_{V_{Li}} = [Li_i] D^*_{Li_i}$ [90].

The second cause of a reduced room-temperature ionic conductivity under subvalent doping is recombination of $\left[V'_{Li} + Li_i^\bullet\right]$ Frenkel pairs when the system is cooled. The $\left[V'_{Li} + Li_i^\bullet\right]$ Frenkel pair formation energy in Li_3OCl is high (our calculated value is $2.6\,eV$), which indicates a strong enthalpic driving force for lithium vacancy–interstitial pairs to recombine. Because lithium vacancies and lithium interstitials recombine in a 1:1 ratio, this Frenkel-pair recombination is limited by the concentration of the minority lithium defect species. In undoped Li_3OCl, the concentration of lithium interstitials is low and lithium vacancies are present in large excess. Frenkel-pair recombination therefore has a negligible effect on the lithium vacancy concentration and a corresponding negligible effect on the net ionic conductivity. Subvalent doping, however, under all synthesis conditions, increases the concentration of lithium interstitials and decreases the concentration of lithium vacancies. As the concentrations of these two defects become more equal, an increasing proportion of lithium vacancies are removed through Frenkel-pair recombination, and the ionic conductivity is progressively reduced. This effect is strongest when the concentrations of lithium vacancies and lithium interstitials are equal; nearly all the lithium vacancies and interstitials recombine, greatly reducing
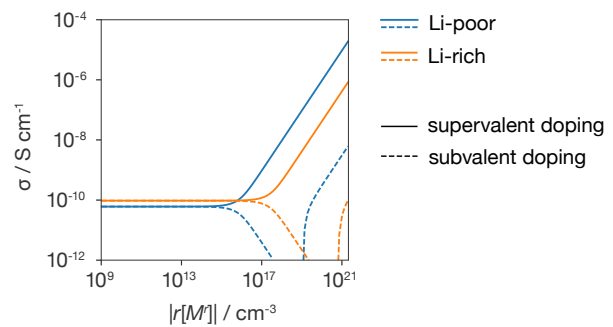
FIG. 7. Predicted room-temperature ionic conductivity of Li_3OCl under Li-rich and Li-poor synthesis conditions as a function of supervalent or supvalent effective dopant concentration, $r\,|M^r|$.

the concentrations of these charge carrying defects, and giving a sharp decrease in ionic conductivity. For effective dopant concentrations above this threshold, the concentration of lithium interstitials under synthesis conditions now exceeds that of lithium vacancies, and the room temperature lithium interstitial concentration and ionic conductivity both increase with effective dopant concentration.

The different ionic conductivity responses to supervalent versus subvalent doping, under lithium-rich and lithium-poor conditions, are compared graphically in fig. 7. As noted above, subvalent doping is predicted to give no net increase in ionic conductivity except at very high dopant levels. Even at sufficient subvalent doping levels to produce a net increase in ionic conductivity, the resulting conductivity increase remains orders of magnitude smaller than for supervalent doping at comparable dopant concentrations, and we conclude, therefore, that subvalent doping to increase lithium interstitial concentrations is not an effective strategy for enhancing the ionic conductivity of Li_3OCl. Our analysis also indicates that subvalent doping will be maximally effective under Li-poor synthesis conditions, due the associated low formation energy of V_{Li}.

IV. SUMMARY AND DISCUSSION

To characterise the native defect chemistry of Li_3OCl, and to quantify the effect of supervalent and subvalent doping on native defect concentrations and on ionic conductivity, we have performed a hybrid density-functional-theory study of the defect chemistry and aliovalent-doping response of Li_3OCl that considers all native vacancy, interstitial, and anion antisite defect species within a self-consistent thermodynamic model. In undoped Li_3OCl, under Li-poor conditions, the dominant negatively defect species is V'_{Li} and the dominant positively charged defect species is $V^\bullet_{Cl}$, which is qualitatively consistent with previous descriptions of Li_3OCl as being

$[V_{Li} + V_{Cl}]$ Schottky-disordered [3, 34, 41, 48]. Under Li-rich conditions, the dominant defect species are O'_{Cl} and V'_{Li}. The change in highest concentration negatively-charged defect from V_{Li} to O_{Cl} illustrates the potential limitations of considering the defect chemistry of solid electrolytes only in terms of simple Schottky or Frenkel-pair defect formation reactions.

Supervalent doping is predicted to most strongly increase the concentrations of both V'_{Li} and O'_{Cl}. The defect species with the higher concentration in the relevant undoped system undergoes the largest increase, and supervalent doping is therefore predicted to most effectively increase the concentration of lithium vacancies under Li-poor synthesis conditions. Subvalent doping principally increases the concentration of chlorine vacancies ahead of lithium interstitials under all considered synthesis conditions, due to the much higher concentration of chlorine vacancies with respect to lithium interstitials in undoped Li_3OCl.

The quantitatively different response of these competing defect species to supervalent or subvalent doping can be characterised in terms of a "doping-response efficiency", η_X, which we define as the change in concentration of a defect species, $\Delta[X]$, for a fixed effective dopant concentration, $r[M^r]$, divided by the change in concentration if the doping response were purely due to defect X in charge state q', i.e.,

$$\eta_X = -\frac{q'\Delta[X]}{r[M^r]}. \quad (13)$$

This gives a measure of how many additional defects of defect species X are introduced or removed per dopant. Figure 8 shows calculated values of η_X for V_{Li} and O_{Cl} with $q' = -1$ and for V_{Cl} and V'_{Li} with $q' = +1$ for an effective dopant concentration of $r[M^r] = \pm 10^{18}\,\text{cm}^{-3}$ for both supervalent and subvalent doping. The calculated values of $\eta_{V_{Li}}$ and η_{Li_i} reflect the strong asymmetry in the doping response of the lithium vacancy and interstitial. Supervalent doping under lithium-poor conditions strongly increases the concentration of lithium vacancies, indicated by $\eta_{V_{Li}} \approx 1$. For supervalent doping under lithium-rich conditions, $\eta_{V_{Li}}$ remains high, but is now smaller than $\eta_{O_{Cl}}$, reflecting the preferential formation of O_{Cl} antisites. For subvalent doping, $\eta_{Li_i} < 10^{-8}$ under all conditions; at these dopant concentrations, subvalent doping has a negligible effect on the concentration of lithium interstitials and instead principally increases the concentration of Cl vacancies ($\eta_{V_{Cl}} \approx 1$). In the case of Li_3OCl, then, the doping-response efficiency, η_X, provides an intuitive description of the strongly asymmetric response to supervalent versus subvalent doping.

One practical consequence of the asymmetric doping response of Li_3OCl is the qualitatively different response of the ionic conductivity under supervalent versus subvalent doping. Supervalent doping produces a monotonic increase in lithium vacancy concentration, and a corresponding monotonic increase in ionic conductivity. Subvalent doping, in contrast, produces a *decrease* in ionic
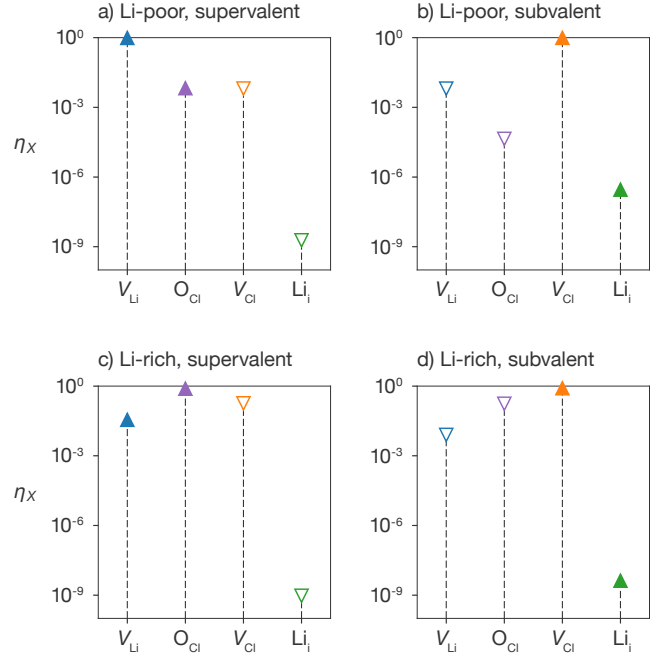
FIG. 8. Doping-response efficiency, η_X, (eq. (13)) for V_{Li}, O_{Cl}, V_{Cl} and Li_i under lithium poor conditions (top row) and lithium rich conditions (bottom row) for supervalent doping (left hand column) and subvalent doping (right hand column) at an effective dopant concentration $r[M^r] = \pm 10^{18}\,\text{cm}^{-3}$. ▲ indicates defect concentrations that increase upon doping, and ▽ indicates defect concentrations that decrease upon doping.

conductivity at low-to-moderate dopant levels due to two complementary effects. First, at low-to-moderate subvalent doping levels the primary effect of subvalent doping is to decrease the concentration of lithium vacancies, rather than increase the concentration of lithium interstitials (cf. fig. 8). Second, by increasing the number of lithium interstitials formed under synthesis conditions, a greater number of lithium vacancies are removed when cooling to room temperature due to recombination of V_{Li} as $[V_{Li} + Li_i]$ Frenkel pairs. For sufficiently high dopant levels, subvalent doping is predicted to give an increase in ionic conductivity relative to undoped Li_3OCl. This net positive contribution to the ionic conductivity, however, only occurs when the effective dopant concentration is much larger than the lithium vacancy concentration in the undoped material, $r[M^r] \gg [V_{Li}]_{undoped}$.

The strongly asymmetric doping response of Li_3OCl with respect to supervalent versus subvalent doping can be understood as a consequence of the low formation energy of positively charged V_{Cl} defects with respect to Li_i defects (fig. 2); equivalently, this effect can be considered to be a consequence of the dominant $[V_{Li} + V_{Cl}]$ Schottky disorder that characterises the lithium defect chemistry in this system. Under Li-poor conditions, the Fermi energy is pinned by the $[V_{Li} + V_{Cl}]$ pair; V_{Li} and V_{Cl} are present in approximately equal concentrations,

and Li_i concentrations are several orders of magnitude lower, corresponding to a classical Schottky-disordered system. Under Li-rich conditions, the Fermi energy is pinned by the $[O_{Cl} + V_{Cl}]$ pair and the dominant defect species are O_{Cl} and V_{Cl} rather than lithium disorder. Under these conditions, however, the concentration of V_{Li} is still several orders of magnitude larger than the concentration of Li_i, and the lithium defect chemistry can still be considered within the schema of $[V_{Li} + V_{Cl}]$ Schottky disorder.

Because the response of a specific defect species to aliovalent doping scales with the concentration of that defect species in the undoped system (eq. 9), Schottky disorder implies a much higher doping-response efficiency, η_X, for V_{Li} than for Li_i—which is indeed the case for Li_3OCl (cf. fig. 8). This leads to $[V_{Li}]$ decreasing much more rapidly than $[Li_i]$ increases under subvalent doping. Schottky disorder also indicates a relatively high $[V_{Li} + Li_i]$ Frenkel pair formation energy, which means a strong enthalpic driving force for Frenkel-pair recombination when cooling from synthesis temperatures to room temperature. Both of the effects that cause ionic conductivity to decrease or only moderately increase in response to subvalent doping are therefore consequences of Li_3OCl being a "Schottky-disordered" solid electrolyte. By extension, we therefore expect other principally Schottky-disordered solid electrolytes, including other antiperovskite solid electrolytes [6, 36, 41–44], to have analogous asymmetric doping responses.

One of the limitations of the study presented here is that we consider dopants as ideal, i.e, they affect the defect chemistry of Li_3OCl only through their effect on the the Fermi energy. In reality, direct dopant–defect interactions may be significant [7, 14, 15, 91]. For example, supervalent dopants, such as Mg^{2+}, are predicted to kinetically trap lithium vacancies [15], which will reduce ionic conductivities relative to the values presented in this work. Despite this limitation, we expect our results to accurately describe quantitative trends for different synthesis conditions and doping strategies for Li_3OCl.

This study also illustrates how the defect chemistry and doping response of solid electrolytes may be more complex than implied by simple mass- and charge-compensating defect formation schemes, and demonstrates how a more complete description that accounts for varying synthesis conditions and thermodynamic competition between defect species can be found by considering a full set of defects within a self-consistent thermodynamic model. Finally, our results show how the defect chemistry and doping response of Li_3OCl can be understood as a consequence of "Schottky-disorder", with quantitatively similar behaviour therefore predicted

for other Schottky-disordered solid electrolytes, including other antiperovskite and structurally-related materials.
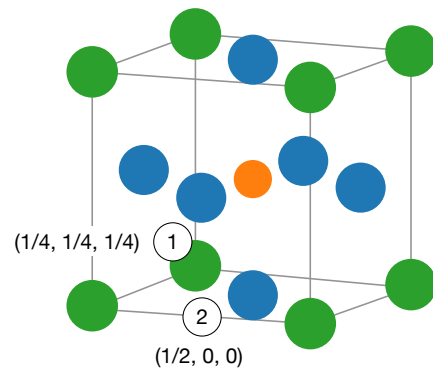
FIG. 9. Initial anion interstitial locations in the Li_3OCl unit cell.

V. SUPPORTING INFORMATION

A. Interstitial positions

Vacancies and antisites have well-defined positions in a periodic crystal, corresponding to atomic positions in the ideal stoichiometric material. In contrast, interstitial sites do not have *a priori* well-defined positions, but instead these must be specified through some additional procedure. In this study, we have considered a total of five interstitial defects, comprising one lithium interstitial, which occupies a "dumbbell" position described by Emly *et al.* [34]; and four anion interstitials, with O or Cl occupying one of two possible sites identified using Voronoi decomposition as implemented in Pymatgen [92] (fig. 9).

ACKNOWLEDGEMENTS

[1] J. Janek and W. G. Zeier, A solid future for battery development, Nat. Energy **1**, 16141 (2016).

[2] T. Famprikis, P. Canepa, J. A. Dawson, M. S. Islam, and C. Masquelier, Fundamentals of inorganic solid-state electrolytes for batteries, Nature Mater. **18**, 1278 (2019).

[3] Y. Zhang, X. He, Z. Chen, Q. Bai, A. M. Nolan, C. A. Roberts, D. Banerjee, T. Matsunaga, Y. Mo, and C. Ling, Unsupervised discovery of solid-state lithium ion conductors, Nature Commun. **10**, 5260 (2019).

[4] L. Kahle, A. Marcolongo, and N. Marzari, High-throughput computational screening for solid-state Li-ion conductors, Energy Environ. Sci. **13**, 928 (2020).

[5] A. Morscher, M. S. Dyer, B. B. Duff, G. Han, J. Gamon, L. M. Daniels, Y. Dang, T. W. Surta, C. M. Robertson, F. Blanc, J. B. Claridge, and M. J. Rosseinsky, $Li_6SiO_4Cl_2$: A hexagonal argyrodite based on antiperovskite layer stacking, Chem. Mater. **33**, 2206 (2021).

[6] S. Fujii, S. Gao, C. Tassel, T. Zhu, T. Broux, K. Okada, Y. Miyahara, A. Kuwabara, and H. Kageyama, Alkali-rich antiperovskite M_3FCh (M = Li, Na; Ch = S, Se, Te): The role of anions in phase stability and ionic transport, J. Am. Chem. Soc. **143**, 10668 (2021).

[7] S. P. Culver, A. G. Squires, N. Minafra, C. W. F. Armstrong, T. Krauskopf, F. Böcher, C. Li, B. J. Morgan, and W. G. Zeier, Evidence for a solid-electrolyte inductive effect in the superionic conductor $Li_{10}Ge_{1-x}Sn_xP_2PS_{12}$, J. Am. Chem. Soc. **142**, 21210 (2020).

[8] B. J. Morgan, Mechanistic origin of superionic lithium diffusion in anion-disordered Li_6PS_5X argyrodites, Chem. Mater. **33**, 2004 (2021).

[9] M. A. Kraft, S. Ohno, T. Zinkevich, R. Koerver, S. P. Culver, T. Fuchs, A. Senyshyn, S. Indris, B. J. Morgan, and W. G. Zeier, Inducing high ionic conductivity in the lithium superionic argyrodites $Li_{6+x}P_{1-x}Ge_xS_5I$ for all-solid-state batteries, J. Am. Chem. Soc. **140**, 16330 (2018).

[10] K. Kim and D. J. Siegel, Correlating lattice distortions, ion migration barriers, and stability in solid electrolytes, J. Mater. Chem. A **7**, 3216 (2019).

[11] J. Goodenough, Ceramic solid electrolytes, Sol. Stat. Ionics **94**, 17 (1997).

[12] Z. Zhu, I.-H. Chu, Z. Deng, and S. P. Ong, Role of Na^+ interstitials and dopants in enhancing the Na^+ conductivity of the cubic Na_3PS_4 superionic conductor, Chem. Mater. **27**, 8318 (2015).

[13] T. Fuchs, S. P. Culver, P. Till, and W. G. Zeier, Defect-mediated conductivity enhancements in $Na_{3-x}Pn_{1-x}W_xS_4$ (Pn = P, Sb) using aliovalent substitutions, ACS Energy Lett. **5**, 146 (2019).

[14] P. Li, F. Hussain, P. Cui, Z. Li, and J. Yang, Boosting ionic conductivity in antiperovskite Li_3OCl via defect engineering: Interstitial versus vacancy, Phys. Rev. Mater. **3**, 115402 (2019).

[15] M. J. Clarke, J. A. Dawson, T. J. Mays, and M. S. Islam, Atomistic insights into the effects of doping and vacancy clustering on Li-ion conduction in the Li_3OCl antiperovskite solid electrolyte, ACS Appl. Energy Mater. **4**, 5094 (2021).

[16] O. Kwon, M. Hirayama, K. Suzuki, Y. Kato, T. Saito, M. Yonemura, T. Kamiyama, and R. Kanno, Synthesis, structure, and conduction mechanism of the lithium superionic conductor $Li_{10+\delta}Ge_{1+\delta}P_{2-\delta}S_{12}$, J. Mater. Chem. A **3**, 438 (2015).

[17] R. Jalem, M. Rushton, W. Manalastas, M. Nakayama, T. Kasuga, J. A. Kilner, and R. W. Grimes, Effects of gallium doping in garnet-type $Li_7La_3Zr_2O_{12}$ solid electrolytes, Chem. Mater. **27**, 2821 (2015).

[18] R. Brugge, J. Kilner, and A. Aguadero, Germanium as a donor dopant in garnet electrolytes, Sol. Stat. Ionics **337**, 154 (2019).

[19] P. Adeli, J. D. Bazak, A. Huq, G. R. Goward, and L. F. Nazar, Influence of aliovalent cation substitution and mechanical compression on Li-ion conductivity and diffusivity in argyrodite solid electrolytes, Chem. Mater. **33**, 146 (2020).

[20] M. A. Kraft, L. M. Gronych, T. Famprikis, and W. G. Zeier, Influence of reduced Na vacancy concentrations in the sodium superionic conductors $Na_{11-x}Sn_2P_{1-x}M_xS_{12}$ (M = Sn, Ge), ACS Appl. Energy Mater. **4**, 7250 (2021).

[21] A. G. Squires, D. O. Scanlon, and B. J. Morgan, Native defects and their doping response in the lithium solid electrolyte $Li_7La_3Zr_2O_{12}$, Chem. Mater. **32**, 1876 (2019).

[22] S. Kim, J. A. Márquez, T. Unold, and A. Walsh, Upper limit to the photovoltaic efficiency of imperfect crystals from first principles, Energy Environ. Sci. **13**, 1481 (2020).

[23] A. Goyal, P. Gorai, S. Anand, E. S. Toberer, G. J. Snyder, and V. Stevanović, On the dopability of semiconductors and governing material properties, Chem. Mater. **32**, 4467 (2020).

[24] M. H. Braga, V. Stockhausen, J. C. Oliveira, and J. A. Ferreira, The role of defects in Li_3ClO solid electrolyte: Calculations and experiments, MRS Proc. **1526**, 905 (2013).

[25] Y. Li, W. Zhou, S. Xin, S. Li, J. Zhu, X. Lü, Z. Cui, Q. Jia, J. Zhou, Y. Zhao, and J. B. Goodenough, Fluorine-doped antiperovskite electrolyte for all-solid-state lithium-ion batteries, Angew. Chem. Int. Edit. **55**, 9965 (2016).

[26] S. Stegmaier, J. Voss, K. Reuter, and A. C. Luntz, Li^+ defects in a solid-state Li ion battery: Theoretical insights with a Li_3OCl electrolyte, Chem. Mater. **29**, 4330 (2017).

[27] Y. Zhao and L. L. Daemen, Superionic conductivity in lithium-rich anti-perovskites, Journal of the American Chemical Society **134**, 15042 (2012).

[28] M. Burbano, D. Carlier, F. Boucher, B. J. Morgan, and M. Salanne, Sparse cyclic excitations explain the low ionic conductivity of stoichiometric $Li_7La_3Zr_2O_{12}$, Phys. Rev. Lett. **116**, 135901 (2016).

[29] B. Kozinsky, S. A. Akhade, P. Hirel, A. Hashibon, C. Elsässer, P. Mehta, A. Logéat, and U. Eisele, Effects of sublattice symmetry and frustration on ionic transport in garnet solid electrolytes, Phys. Rev. Lett. **116**, 055901 (2016).

[30] S. Ohno, A. Banik, G. F. Dewald, M. A. Kraft, T. Krauskopf, N. Minafra, P. Till, M. Weiss, and W. G. Zeier, Materials design of ionic conductors for solid state batteries, Prog. Ener. **2**, 022001 (2020).

[31] B. Kozinsky, Transport in frustrated and disordered solid electrolytes, in *Handbook of Materials Modeling* (Springer International Publishing, 2018) pp. 1–20.

[32] L. Zhou, N. Minafra, W. G. Zeier, and L. F. Nazar, Innovative approaches to Li-argyrodite solid electrolytes for all-solid-state lithium batteries, Acc. Chem. Res. **54**, 2717 (2021).

[33] Y. Zhang, Y. Zhao, and C. Chen, *Ab initio* study of the stabilities of and mechanism of superionic transport in lithium-rich antiperovskites, Phys. Rev. B **87**, 134303 (2013).

[34] A. Emly, E. Kioupakis, and A. Van der Ven, Phase stability and transport mechanisms in antiperovskite Li_3OCl and Li_3OBr superionic conductors, Chem. Mater. **25**,

4663 (2013).

[35] Z. Deng, B. Radhakrishnan, and S. P. Ong, Rational composition optimization of the lithium-rich $Li_3OCl_{1-x}Br_x$ anti-perovskite superionic conductors, Chem. Mater. **27**, 3749 (2015).

[36] Z. Wang, H. Xu, M. Xuan, and G. Shao, From anti-perovskite to double anti-perovskite: tuning lattice chemistry to achieve super-fast Li^+ transport in cubic solid lithium halogen-chalcogenides, J. Mater. Chem. A **6**, 73 (2018).

[37] R. Mouta, M. A. B. Melo, E. M. Diniz, and C. W. A. Paschoal, Concentration of charge carriers, migration, and stability in Li_3OCl solid electrolytes, Chem. Mater. **26**, 7137 (2014).

[38] Z. Lu, C. Chen, Z. M. Baiyee, X. Chen, C. Niu, and F. Ciucci, Defect chemistry and lithium transport in Li_3OCl anti-perovskite superionic conductors, Phys. Chem. Chem. Phys. **17**, 32547 (2015).

[39] M. H. Braga, J. A. Ferreira, V. Stockhausen, J. E. Oliveira, and A. El-Azab, Novel Li_3ClO based glasses with superionic properties for lithium batteries, J. Mater. Chem. A **2**, 5470 (2014).

[40] M. H. Braga, N. S. Grundish, A. J. Murchison, and J. B. Goodenough, Alternative strategy for a safe rechargeable battery, Energy Environ. Sci. **10**, 331 (2017).

[41] J. A. Dawson, H. Chen, and M. S. Islam, Composition screening of lithium- and sodium-rich anti-perovskites for fast-conducting solid electrolytes, J. Phys. Chem. C **122**, 23978 (2018).

[42] T. H. Wan, Z. Lu, and F. Ciucci, A first principle study of the phase stability, ion transport and substitution strategy for highly ionic conductive sodium antipervoskite as solid electrolyte for sodium ion batteries, J. Power Sources **390**, 61 (2018).

[43] J. Dawson, T. Famprikis, and K. E. Johnston, Anti-perovskites for solid-state batteries: Recent developments, current challenges and future prospects, J. Mater. Chem. A 10.1039/d1ta03680g (2021).

[44] S. Gao, T. Broux, S. Fujii, C. Tassel, K. Yamamoto, Y. Xiao, I. Oikawa, H. Takamura, H. Ubukata, Y. Watanabe, K. Fujii, M. Yashima, A. Kuwabara, Y. Uchimoto, and H. Kageyama, Hydride-based antiperovskites with soft anionic sublattices as fast alkali ionic conductors, Nat. Commun **12**, 10.1038/s41467-020-20370-2 (2021).

[45] S. Zhang and J. Northrup, Chemical potential dependence of defect formation energies in GaAs: Application to Ga self-diffusion, Phys. Rev. Lett. **67**, 2339 (1991).

[46] J. Buckeridge, Equilibrium point defect and charge carrier concentrations in a material determined through calculation of the self-consistent Fermi energy, Comp. Phys. Commun. **244**, 329 (2019).

[47] M. Wu, B. Xu, X. Lei, K. Huang, and C. Ouyang, Bulk properties and transport mechanisms of a solid state antiperovskite Li-ion conductor Li_3OCl: insights from first principles calculations, J. Mater. Chem. A **6**, 1150 (2018).

[48] A. Baktash, B. Demir, Q. Yuan, and D. J. Searles, Effect of defects and defect distribution on Li-diffusion and elastic properties of anti-perovskite Li_3OCl solid electrolyte, Energy Stor. Mater. **41**, 614 (2021).

[49] N. W. Ashcroft, *Solid State Physics* (Cengage Learning, 1976).

[50] S. Lany and A. Zunger, Assessment of correction methods for the band-gap problem and for finite-size effects in supercell defect calculations: Case studies for ZnO and GaAs, Phys. Rev. B **78**, 17 (2008).

[51] C. Kittel, *Thermal physics* (W.H. Freeman, San Francisco, 1980).

[52] G. Kresse and J. Furthmüller, Efficient iterative schemes for ab initio total-energy calculations using a plane-wave basis set, Phys. Rev. B. **54**, 11169 (1996).

[53] G. Kresse and J. Furthmüller, Efficiency of ab-initio total energy calculations for metals and semiconductors using a plane-wave basis set, Comput. Mater. Sci. **6**, 15 (1996).

[54] A. V. Krukau, O. A. Vydrov, A. F. Izmaylov, and G. E. Scuseria, Influence of the exchange screening parameter on the performance of screened hybrid functionals, J. Chem. Phys. **125** (2006).

[55] P. Borlido, T. Aull, A. W. Huran, F. Tran, M. A. L. Marques, and S. Botti, Large-scale benchmark of exchange–correlation functionals for the determination of electronic band gaps of solids, J. Chem. Theor. Comput. **15**, 5069 (2019).

[56] D. O. Scanlon, B. J. Morgan, and G. W. Watson, Modeling the polaronic nature of p-type defects in Cu_2O: The failure of GGA and GGA+U, J. Chem. Phys. **131**, 124703 (2009).

[57] B. J. Morgan, D. O. Scanlon, and G. W. Watson, The use of the "+U" correction in describing defect states at metal oxide surfaces: Oxygen vacancies on CeO_2 and TiO_2, and Li-doping of MgO, e-J. Surf. Sci. Nanotech. **7**, 389 (2009).

[58] P. Deák, B. Aradi, and T. Frauenheim, Polaronic effects in TiO_2 calculated by the HSE06 hybrid functional: Dopant passivation by carrier self-trapping, Phys. Rev. B **83**, 155207 (2011).

[59] B. J. Morgan and G. W. Watson, Polaronic trapping of electrons and holes in anatase TiO_2, Phys. Rev. B **80**, 233102 (2009).

[60] P. E. Blöchl, Projector augmented-wave method, Phys. Rev. B **50**, 17953 (1994).

[61] F. D. Murnaghan, The Compressibility of Media under Extreme Pressures, Proc. Natl. Acad. Sci. **30**, 244 (1944).

[62] awaiting doi.

[63] A. G. Squires, supporting code, `github.com/alexsquires/defects_in_antiperovskites`.

[64] P. Virtanen, R. Gommers, T. E. Oliphant, M. Haberland, T. Reddy, D. Cournapeau, E. Burovski, P. Peterson, W. Weckesser, J. Bright, S. J. van der Walt, M. Brett, J. Wilson, K. J. Millman, N. Mayorov, A. R. J. Nelson, E. Jones, R. Kern, E. Larson, C. J. Carey, İ. Polat, Y. Feng, E. W. Moore, J. VanderPlas, D. Laxalde, J. Perktold, R. Cimrman, I. Henriksen, E. A. Quintero, C. R. Harris, A. M. Archibald, A. H. Ribeiro, F. Pedregosa, P. van Mulbregt, and SciPy 1.0 Contributors, enSciPy 1.0: fundamental algorithms for scientific computing in python, Nat. Methods **17**, 261 (2020).

[65] C. R. Harris, K. J. Millman, S. J. van der Walt, R. Gommers, P. Virtanen, D. Cournapeau, E. Wieser, J. Taylor, S. Berg, N. J. Smith, R. Kern, M. Picus, S. Hoyer, M. H. van Kerkwijk, M. Brett, A. Haldane, J. F. Del Río, M. Wiebe, P. Peterson, P. Gérard-Marchant, K. Sheppard, T. Reddy, W. Weckesser, H. Abbasi, C. Gohlke, and T. E. Oliphant, enArray programming with NumPy, Nature **585**, 357 (2020).

[66] W. McKinney, Data structures for statistical computing in python, in *Proceedings of the 9th Python in Science Conference* (SciPy, 2010).

[67] J. D. Hunter, Matplotlib: A 2D graphics environment, Comput. Sci. Eng. **9**, 90 (2007).

[68] B. J. Morgan, A. G. Squires, py-sc-fermi, `https://github.com/bjmorgan/py-sc-fermi`.

[69] J. Buckeridge, D. O. Scanlon, A. Walsh, and C. R. Catlow, Automated procedure to determine the thermodynamic stability of a material and the range of chemical potentials necessary for its formation relative to competing phases and compounds, Comput. Phys. Comm. **185**, 330 (2014).

[70] M.-H. Chen, A. Emly, and A. Van der Ven, Anharmonicity and phase stability of antiperovskite Li_3OCl, Phys. Rev. B **91**, 214306 (2015).

[71] J. A. S. Serejo, J. S. S. Pereira, R. Mouta, and L. G. C. Rego, Sluggish anion transport provides good kinetic stability to the anhydrous anti-perovskite solid electrolyte Li_3OCl, Phys. Chem. Chem. Phys. **23**, 6964 (2021).

[72] While synthesis temperatures are typically reported in experimental studies, gas phase partial pressures are not, so to be certain we capture a wide range of synthesis conditions, we consider all oxygen partial pressures from atmospheric conditions through to 1×10^{-10} atm.

[73] *CRC Handbook of Chemistry and Physics, 100th Edition* (CRC Press, 2019).

[74] M. Finnis, A. Lozovoi, and A. Alavi, The oxidation of NiAl: What can we learn from ab initio calculations?, Annu. Rev. Mater. Res. **35**, 167 (2005).

[75] B. J. Morgan and G. W. Watson, Intrinsic n-type defect formation in TiO_2: A comparison of rutile and anatase from GGA+U calculations, J. Phys. Chem. C **114**, 2321 (2010).

[76] S. Hull, D. A. Keen, P. A. Madden, and M. Wilson, Ionic diffusion within the α^* and β phases of Ag_3SI, J. Phys.: Condens. Matter **19**, 406214 (2007).

[77] M. Gombotz, I. Hanghofer, S. Eisbacher-Lubensky, and H. Wilkening, Ionic and electronic transport in the fast Ag conductor α^*-Ag_3SI, Sol. Stat. Sci. **118**, 106680 (2021).

[78] A. Gautam, M. Sadowski, M. Ghidiu, N. Minafra, A. Senyshyn, K. Albe, and W. G. Zeier, Engineering the site-disorder and lithium distribution in the lithium superionic argyrodite Li_6PS_5Br, Adv. Energy Mater. **11**, 2003369 (2020).

[79] M. Sadowski and K. Albe, Influence of Br^-/S^{2-} site-exchange on Li diffusion mechanism in Li_6PS_5Br – a computational study (2021), arXiv:2102.09873 [cond-mat.mtrl-sci].

[80] The concentration of $r[M^r] = 10^{18}$ cm^{-3} corresponds to approximately 4 in 10^7 sites occupied by a dopant atom.

[81] A. Gray-Weale and P. A. Madden, Dynamical arrest in superionic crystals and supercooled liquids, J. Phys. Chem. B **108**, 6624 (2004).

[82] A. Gray-Weale and P. A. Madden, The energy landscape of a fluorite-structured superionic conductor, J. Phys. Chem. B **108**, 6634 (2004).

[83] B. J. Morgan, Lattice-geometry effects in garnet solid electrolytes: a lattice-gas Monte Carlo simulation study, R. Soc. Open Sci. **4**, 170824 (2017).

[84] R. E. Howard and A. B. Lidiard, Matter transport in solids, Rep. Prog. Phys. **27**, 161 (1964).

[85] K. Sasaki and J. Maier, Low-temperature defect chemistry of oxides. I. general aspects and numerical calculations, J. Appl. Phys. **86**, 5422 (1999).

[86] A. Squires, D. Davies, S. Kim, D. Scanlon, A. Walsh, and B. J. Morgan, Low Electronic Conductivity of $Li_7La_3Zr_2O_{12}$ (LLZO) Solid Electrolytes from First Principles 10.26434/chemrxiv.13154297.v1 (2020).

[87] X. Lü, G. Wu, J. W. Howard, A. Chen, Y. Zhao, L. L. Daemen, and Q. Jia, Li-rich anti-perovskite Li_3OCl films with enhanced ionic conductivity, Chem. Commun. **50**, 11520 (2014).

[88] I. Hanghofer, G. J. Redhammer, S. Rohde, I. Hanzu, A. Senyshyn, H. M. R. Wilkening, and D. Rettenwander, Untangling the structure and dynamics of lithium-rich anti-perovskites envisaged as solid electrolytes for batteries, Chem. Mater. **30**, 8134 (2018).

[89] J. A. Dawson, T. S. Attari, H. Chen, S. P. Emge, K. E. Johnston, and M. S. Islam, Elucidating lithium-ion and proton dynamics in anti-perovskite solid electrolytes, Energy Environ. Sci. **11**, 2993 (2018).

[90] J. Maier, *Physical Chemistry of Ionic Materials* (John Wiley & Sons, Ltd, 2004).

[91] M. Mottet, A. Marcolongo, T. Laino, and I. Tavernelli, Doping in garnet-type electrolytes: Kinetic and thermodynamic effects from molecular dynamics simulations, Phys. Rev. Mater. **3**, 035403 (2019).

[92] S. P. Ong, W. D. Richards, A. Jain, G. Hautier, M. Kocher, S. Cholia, D. Gunter, V. L. Chevrier, K. A. Persson, and G. Ceder, Python Materials Genomics (pymatgen): A robust, open-source Python library for materials analysis, Comput. Mater. Sci. **68**, 314 (2013).